International Journal of Heat and Mass Transfer 51 (2008) 5552–5561

Contents lists available at ScienceDirect

International Journal of Heat and Mass Transfer

journal homepage: www.elsevier.com/locate/ijhmt

Transport profiles in the conducting airways of the human lung

F.E. Fresconi [a], A.S. Wexler [b,1], A.K. Prasad [a,*]

[a] Department of Mechanical Engineering, University of Delaware, Newark, DE 19716, United States
[b] Departments of Mechanical and Aeronautical Engineering, Civil and Environmental Engineering, and Land, Air, and Water Resources, University of California, Davis, CA 95616, United States

ARTICLE INFO

Article history:
Received 4 October 2007
Received in revised form 4 April 2008
Available online 5 June 2008

Keywords:
Transport profile
Aerosol transport
Dispersion
Drug delivery
Steady streaming

ABSTRACT

Transport in the conducting region of the human airways affects many diagnostic and therapeutic procedures. In this work, convective mass transport is characterized by a transport profile that is used to (1) investigate the significance of simple streaming and augmented dispersion mechanisms, and (2) understand steady streaming in the human airways. Laser-induced fluorescence experiments and numerical simulations were performed to assess transport profiles on inspiration and expiration for a range of Reynolds numbers at various locations in a three-generation model of the conducting region of the lung. The shape of the transport profile was found to be largely independent of generation, branch, flow direction, and Reynolds number. Simple streaming was relatively more important to convective dispersion than augmented dispersion. An alternative explanation for steady streaming, based on geometric asymmetries associated with a bifurcation network, is presented.

1. Introduction

Convective dispersion in the lung is due to the mixing and dilution of mass – gas or aerosol – with residual air in the lung caused by bulk motion of the host fluid. Understanding dispersion mechanisms in the human lung aids the clinical diagnosis of lung function [1], facilitates the design of therapeutic aerosols and devices for pulmonary drug delivery [2], improves risk assessment due to inhalation of atmospheric pollutants and exhalation of harmful bio-aerosols [3–5], and helps explain alternative modes of ventilation, such as high-frequency ventilation [6]. In the aerosol bolus technique [7,8], the subject inhales a narrow bolus of particles with low intrinsic mobility. Convective dispersion can be characterized by recovering the bolus upon expiration; when represented as a concentration curve, the bolus broadens to occupy a larger volume and exhibits asymmetry.

Alternative modes of ventilation are often employed to promote gas exchange during injury or illness. High-frequency ventilation (HFV) [6] is one such method that produces small pressure variations (essential for weakened individuals) while still maintaining ventilation by performing small volume oscillations at a high frequency. The mechanism by which such ventilation occurs is not clearly understood since the inspired volumes for HFV are smaller than the dead space (non-gas-exchanging region).

In the present work, three convective dispersion mechanisms are addressed: simple streaming, augmented dispersion, and steady streaming. The displacement of a bolus into a given airway by an azimuthally and radially varying axial component of velocity is denoted as simple streaming.

Augmented dispersion differs from simple streaming due to the presence of a significant amount of cross-sectional mixing by secondary flow activity [9]. Centrifugal effects produce well-ordered secondary vortices for the flow in a curved tube beyond a critical Dean number $\left(Dn = Re\sqrt{\frac{d/2}{\Re}}\right)$, where Re is the Reynolds number, d is the tube diameter, and $\Re$ is the local radius of curvature [10,11]. Secondary currents mix solute in the cross section. Thus, augmented dispersion is the mechanism by which a bolus of passive tracer not only displaces into a given airway by primary (axial) motion but also redistributes within the cross section due to secondary (lateral) activity.

Steady streaming is the non-zero displacement of species in an oscillatory flow. Flow visualization experiments performed in bifurcation models confirmed the existence of steady streaming in the respiratory tract for relatively low frequency oscillations at approximately $1 < Re < 1000$ [12,13]. Solute originally near the tube centerline moved away from the "mouth" and that near the lumen progressed toward the "mouth" after an integer number of cycles. The difference in velocity profiles on inspiration and expiration was offered to explain this phenomenon [12,13]. This explanation must be revisited due to two factors. Arguments based on the Eulerian description of the flow (i.e., differences in velocity profiles) cannot fully elucidate mass transport. An investigation

* Corresponding author. Tel.: +1 302 831 2960; fax: +1 302 831 3619.
E-mail addresses: fresconi@udel.edu (F.E. Fresconi), aswexler@ucdavis.edu (A.S. Wexler), prasad@udel.edu (A.K. Prasad).
[1] Tel.: +1 530 754 6558; fax: +1 530 754 8771.

0017-9310/$ - see front matter © 2008 Elsevier Ltd. All rights reserved.
doi:10.1016/j.ijheatmasstransfer.2008.04.014

Nomenclature

A	cross-sectional area
C	concentration
D	diffusivity
Dn	Dean number
G	generation
O	opposite secondary velocity direction
Pe	Peclet number
Q	volume flow rate
$\Re$	radius of curvature
Re	Reynolds number
S	same secondary velocity direction
Sc	Schmidt number
V	volume between initial disk and interrogation station
X	axial width of disk or bolus
d	diameter
n	polynomial order
r	radial coordinate
t	time
u	flow velocity
x	location of bolus front

Greek symbols

ν	kinematic viscosity

Subscripts

G	generation
m	mean
mol	molecular
o	initial

Superscript

*	*non-dimensionalized*

based on tracer transport profiles (Lagrangian description) would be more beneficial. Also, while steady streaming has been experimentally confirmed in bifurcations at $Re \sim 1$, velocity fields have not been measured at these low Re values. It remains unclear whether inertial effects are large enough to produce velocity profiles at $Re \sim 1$ that are any different than Poiseuille flow for both inspiration and expiration. Another explanation may be necessary to fully characterize steady streaming in the airways.

Simulations [14] and experiments [15] have provided additional insight into steady streaming in the lung. It was found that some solute remained anchored at each carina after transiting the bifurcation due to the no-slip boundary condition as the bolus tip impacted the carinal ridge. The net effect after a complete cycle is to displace solute originally near the centerline of the parent tube more distally. This observation agrees with the steady streaming visualizations of Haselton and Scherer [12,13]. The overall influence of this phenomenon on the steady streaming mechanism in the lung has not been adequately emphasized.

In this work, experiments and numerical simulations were employed to evaluate the Lagrangian mass transport profiles in the conducting region of the lung. Mass transport profiles were used to (1) investigate the significance of simple streaming and augmented dispersion mechanisms, and (2) understand steady streaming in the human airways. Laser-induced fluorescence (LIF) measurements at various Re on inspiration and expiration captured the temporal evolution of a bolus of passive tracer in a three-generation model of the airways. Companion numerical simulations allowed mapping of the experimental response curves to a well-described concentration distribution. A benchmark exercise was conducted to ensure proper calibration of experimental and numerical results. The Re range ($10 < Re < 100$) implemented in this study corresponded to approximately symmetric Weibel generations 7–13 at normal respiration [16,17].

2. Experiments

2.1. Model and methods

The geometry used in the three-generation model, shown in Fig. 1 for the largest bifurcation unit, is consistent with that given for the conducting airways by Pedley [16]. The diameter ratio from parent to daughter tubes is 0.78. Centerlines of daughter tubes are separated by a 70° angle. The length-to-diameter ratio of a given airway is 3.5. The radius of curvature of the bifurcation is 7.5 times the parent tube radius.

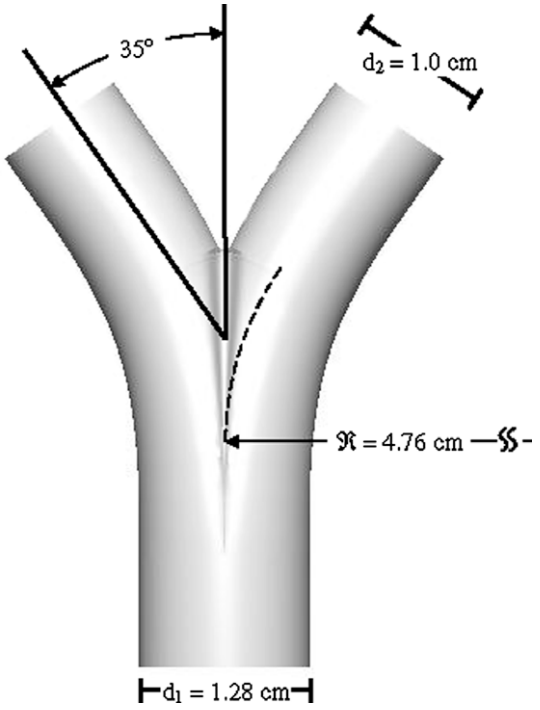

Fig. 1. Bifurcation geometry and dimensions for largest bifurcation unit.

A complete three-generation model of the conductive airways was manufactured in a transparent elastomer (Dow Sylgard 184). The plane containing the axes of the parent and daughter tubes (bifurcation plane) was kept the same for all generations. The fabrication technique, detailed in Hopkins' paper [18], employed a rapid prototyping machine to produce a water-soluble negative of the bifurcation tree; the negative was then used as a pattern in a casting process to retrieve the desired positive of the airway geometry in transparent elastomer.

A schematic of the in-plane bifurcation tree is presented in Fig. 2. Nomenclature for the inspiration experiments is given on the right and that for expiration on the left. Generation (G) is counted based on the number of bifurcations that the flow has passed through on inhalation; this sequence reverses for expiration. The particular branch at a given generation must also be specified due to the influence of centrifugal effects. After transiting a

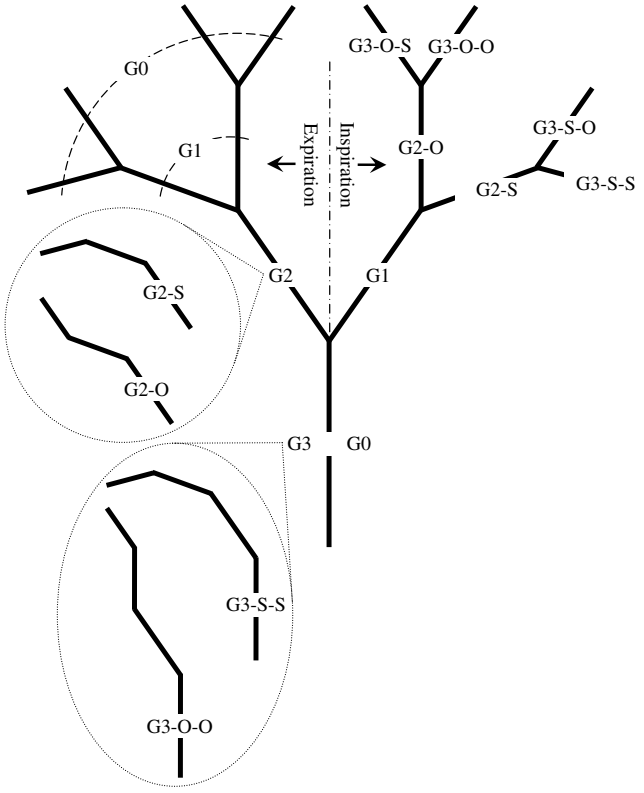

Fig. 2. Schematic of three-generational model geometry with nomenclature.

single generation, secondary currents with a predictable direction may exist. When this flow encounters the subsequent generation, centrifugal effects due to the local curvature at that generation may reinforce or weaken the incoming secondary activity. In an in-plane model, the center of curvature may be used as a metric to determine whether secondary currents of the same direction (*S*) will persist, or if secondary currents of an opposite direction (*O*) may be expected. The *S* case represents the maximum of lateral mixing (most vigorous secondary velocity) and, therefore, minimal axial dispersion. Conversely, the *O* case characterizes the opposite end of this spectrum; minimal lateral mixing (least vigorous secondary velocity) and maximum axial dispersion. An out-of-plane bifurcation model (such as one in which the bifurcation planes of successive generations rotate by 90°) would exhibit secondary flow mixing that lies between these extremes (i.e., between the *S* and *O* cases). In this manner, the effect of the *S* and *O* cases on mixing was assessed.

The schematic identifies *S* and *O* cases based on the history of the flow through each generation. For example, an inspiration labeled *G3-O-O* has passed through three generations and had the local secondary currents change direction at the second and third generations. Likewise, *G3-S-S* on expiration has encountered the same local centrifugal effects at the second and third generations. The insets in Fig. 2 for expiration fully cover all cases that were measured.

The experimental set-up is shown in Fig. 3. The refractive index of the working fluid (58% by weight glycerol and 42% water) was matched to that of the elastomer model to remove optical distortion during measurements. The working fluid was housed in a reservoir that was connected to the model by flexible tubing. A total of eight terminal daughter tubes exited the model and were each connected with flexible tubing to a set of syringes. These syringes were mounted on a translation stage coupled with a stepper motor to allow precise control of the flow through the model.

A Continuum Surelite II Nd:YAG pulsed laser beam (120 mJ/pulse at 532 nm) was used for LIF experiments. Sheet-forming and steering optics illuminated prescribed cross sections of the bifurcation model. A LaVision Imager Intense (10 bit, 1376 × 1040 pixels) camera was oriented perpendicular to the light sheet. A filter was placed in front of the camera lens to block elastic light scattering by the apparatus while passing fluorescence from the dye bolus (Rhodamine 6*G*). The dye was injected through a small-bore hole in the wall of the tubes. While several injection methods were evaluated, this technique was found to produce the most ideal, reproducible bolus. The high Schmidt number ($\sim 10^3$), $\left(Sc = \frac{\nu}{D_{\mathrm{mol}}}\right)$ where ν is the kinematic viscosity and D_{mol} is the molecular, or Brownian diffusivity, of Rhodamine 6*G* in the working fluid, along with the relatively small time-scale during experiments, guaranteed that the molecular diffusion of the dye was negligible. Two bolus sizes, small and large, were utilized in experiments. Assuming the dye filled the interior volume as a cylinder, the small and large boluses corresponded to axial lengths of two and six local diameters, respectively. The bolus size did not influence results; therefore, small and large bolus measurements were averaged in the final results.

Dye was injected at the entrance to the bifurcation tree prior to the start of the flow. The laser sheet and camera were positioned at the desired cross section of a given generation and branch of the model. Images were recorded after initiation of the flow. In this manner, the intensity and spatial distribution of the bolus in the cross section of the tube was captured as a function of time. Qualitative observations from these experimental flow visualizations are given in the next section. Preliminary experiments ensured that the intensity of dye was linearly related to the concentration. Thus, the cross-sectional average of bolus concentration was obtained by computing the average intensity in the frame. Average bolus concentration as a function of time (response curve) was normalized by the peak value of concentration. The standard deviation of the response curve, a representation of the convective dispersion and kinematics of the flow, was calculated. Multiple trials with the same set of experimental variables were conducted and the uncertainty based on the standard deviation was used to determine the ensemble size. An example of experimental response curves is shown in Fig. 4. Data points for multiple trials of a particular experimental condition are shown, along with the associated average curve and uncertainty bounds. Data with magnitude less than 15% of the maximum value was not analyzed [7].

The independent experimental variables were generation, branch, flow direction, and *Re*. Measurements of concentration at generations 1–3, including at various branches at a particular generation, allowed the study of the influence of history on mass

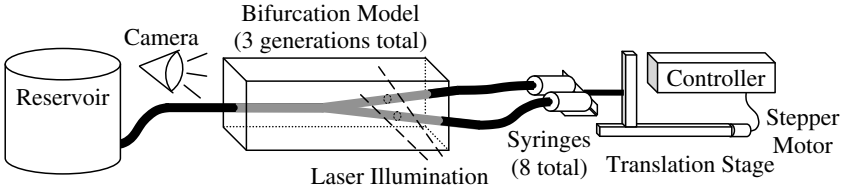

Fig. 3. Experimental set-up.

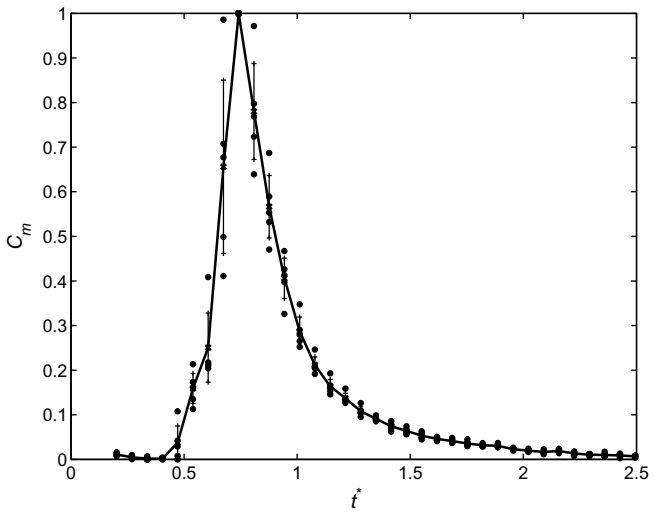

Fig. 4. Typical normalized mean concentration as a function of non-dimensional time from experiments. Circles represent data from multiple trials. Curve gives average of all trails, along with associated uncertainty bands at 95% confidence level.

transport in the conducting region of the lung. The main qualitative difference between inspiration and expiration were that two and four secondary currents were observed, respectively, due to centrifugal forces, as has been observed previously [10,11,19,20]. Two *Re* values, low ($Re \approx 10$) and high ($Re \approx 100$), explored the impact of secondary current pattern and strength on convective dispersion.

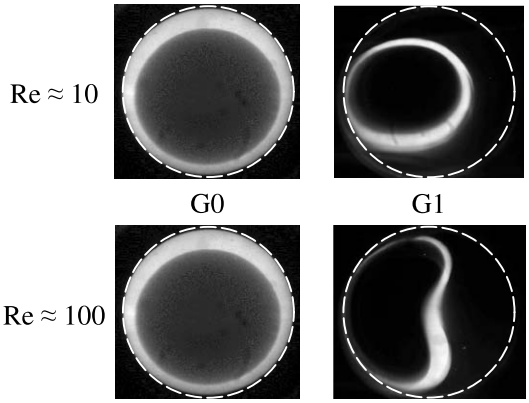

Fig. 5. Flow visualizations on inspiration at low and high *Re* before (*G*0) and after (*G*1) one generation.

2.2. Qualitative experimental observations

As explained in the previous section, LIF measurements captured the temporal evolution of the deformation pattern of dye in the cross section of a given branch of the model on inspiration and expiration at various *Re* numbers. A sample of this data is shown in Figs. 5 and 6 to provide qualitative information regarding transport in the conducting airways. The plane containing the axis of parent and daughter tubes (bifurcation plane) is oriented horizontally in all images. Refer to Fig. 2 for a description of measurement location and upstream branch history for each image (e.g., *G*0, *G*1, *G*2-*O*, *G*2-*S*) on inspiration and expiration.

Inspiring flow visualizations are presented in Fig. 5 for $Re \approx 10$ (top row) and $Re \approx 100$ (bottom row). Images on the left were obtained at *G*0 and those to the right at *G*1. Note that *G*0 images are for a straight tube (bolus has not yet traversed a bifurcation) and therefore represent Poiseuille flow. The annular dye pattern captured for *G*0 is typical of Poiseuille flow. The bolus is deformed into a paraboloid of revolution and a cross-sectional slice reveals an annular band whose radius and thickness are related to the duration of the flow and the initial axial thickness of the bolus. *G*0 images for $Re \approx 10$ and ≈ 100 are repeated to illustrate that, in these experiments as in theory, the kinematics of Poiseuille flow are independent of *Re* number. The annulus shown for *G*1 at low *Re* is skewed slightly off the tube centerline due to the impact of the paraboloid of revolution from *G*0 on the carina at the first bifurcation. For higher *Re* at *G*1 (bottom-right), however, a double vortex due to centrifugal effects is apparent as the dye assumes a kidney shape. Note that the stretched bolus extends all the way from the centerline to the wall for all inspiration flow visualizations. In contrast, the bolus on expiration will be shown to occupy only a portion of the cross section.

Fig. 6 shows representative dye patterns at low *Re* (top row) and high Re (bottom row) for various generations and branch histories on expiration. Again, *G*0 images represent Poiseuille flow. Upon traversing one generation at low *Re*, a half-moon structure appears (top-second from left) because two daughter streams have merged and only one has been dyed. Symmetry has been preserved about a plane normal to the bifurcation plane and containing the axis of the local parent tube (normal plane). The pattern is similar for *G*1 at high *Re* (bottom-second from left), however, a quadruple vortex due to centrifugal effects is evident. Flow visualizations for *G*2 expound on these phenomena. The elongated structure for *G*2-*O* at low *Re* (top-third from left) is wrapped into a "C" shape by centrifugal effects at high *Re* (bottom-third from left). This finding is similar to *G*2-*S*, where an annular formation at low *Re* (top-right) is also deformed into a more "C"-shaped region at high *Re* (bottom-right) by centrifugal effects.

Flow visualizations for expiration after two and three generations at low *Re* number show that dye is constrained to occupy par-

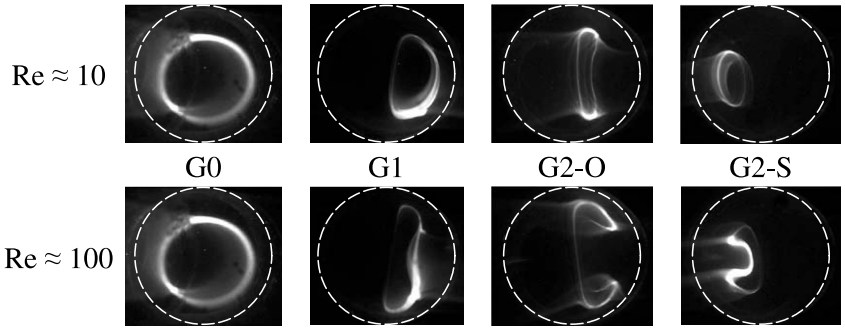

Fig. 6. Flow visualizations on expiration at low and high *Re* at various locations in the bifurcation tree. Refer to Fig. 2 for nomenclature (*G*0, *G*1, *G*2-*O*, *G*2-*S*) associated with measurement location.

ticular regions of the cross section prescribed by the total number of daughter tubes merging and the specific daughter tube into which the dye was injected. At high *Re* number, however, centrifugal effects serve to distribute the incoming dye largely over the entire half cross section at each merge. These dye-containing regions for expiration at low and high *Re* are in contrast to a complete fill of the cross section with dye for inspiration and provide key guidelines for the subsequent analysis of transport profiles for the conducting airways. The model for bolus response curve analysis is described next.

3. Theoretical modeling and numerical methods for application to experiments

3.1. Model introduction

Bolus dispersion measurements on human subjects show penetration beyond the tidal volume [7,8]. Inhaled boluses do not transport into the lung by maintaining a step-function in concentration with the front located precisely at the interface between tidal and residual volume. Rather, friction acting on the bolus at the lumen modifies the bolus front such that it assumes a curved shape. Consequently, for a given inhaled volume, concentration decreases monotonically with lung depth. This curved shape, with zero displacement at the wall and a peak at the centerline, taken by the bolus front in the axial direction is revealed by the flow visualizations of Haselton and Scherer [12,13] and the simulations of Lee and Lee [14]. The resultant shape taken by the bolus front at a given lung depth in this situation can be modeled with an *n*th order polynomial. More specifically, the front of the bolus (x) in a specific airway is assumed to be characterized by

$$x = \left(\frac{n+2}{n}\right)\frac{Qt}{A}\left(1-\left(\frac{r}{d/2}\right)^{n}\right) \tag{1}$$

where n is the order of the polynomial, Q is the volume flow rate, t is the time, A is the cross-sectional area of the tube, and r is the radial coordinate. Nominal transport profiles for polynomials of order 1, 2, 3, and 4 are shown in Fig. 7. Note that more pointed transport profiles correspond to lower polynomial orders, and vice versa; $n = 2$ corresponds to a parabolic profile (Poiseuille flow).

This equation matches observations of bolus dispersion measurements on human subjects and satisfies both mass conservation and the no-slip boundary condition at the lumen. This formulation allows investigation of dispersion mechanisms at the generation and branch level, whereas the bolus dispersion technique for human subjects lumps all dispersion phenomena over a breathing cycle and throughout the respiratory tract. An understanding of the shape of the transport profile in the lung permits assessment of the penetration depth of a bolus.

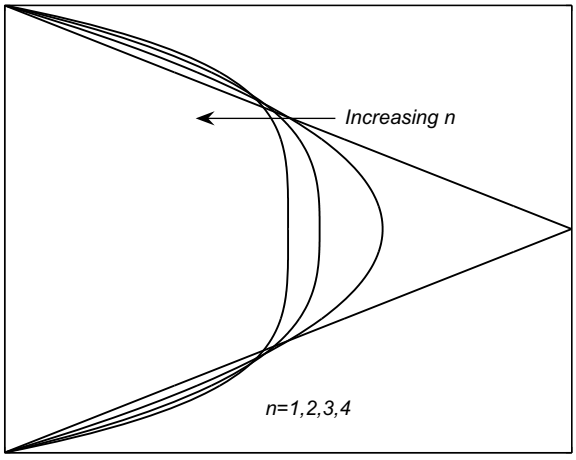

Fig. 7. Sample transport profiles from *n*th order polynomial model. Note how transport profile changes from pointed to blunted as n increases from 1 to 4.

This modeling approach has been used previously. Park and Wexler [21] employed an effective *n*th order polynomial transport profile on inspiration and expiration to account for convective dispersion during a single breath. The dispersion metrics from their model matched those from several experimental studies.

It is important to note that the metric of interest here is the mass transport profile, not the velocity profile. Investigation of the velocity profile in the airways can be found elsewhere [10,11]. The transport profile is of greater value to the study of convective dispersion. For this reason, the mass transport profile paradigm is followed throughout in the present effort.

Eq. (1) can be used along with an initial distribution of solute to arrive at the concentration distribution as a function of time at some downstream station. Taylor [22] solved for the cross-sectional average concentration (C_m) of an initial disk of solute as a function of time in Poiseuille flow due to convection alone to find

$$C_m = \frac{XA}{2Qt}, \tag{2}$$

where X is the initial axial width of the disk.

Taylor's result can be extended for the *n*th order polynomial, as given below

$$C_m = \frac{2XA}{(n+2)Qt}\left(1-\frac{V}{\left(\frac{n+2}{n}\right)Qt}\right)^{\frac{2-n}{n}}, \tag{3}$$

where V is the volume between the initial disk and interrogation station. Eq. (3) reduces to Eq. (2) for $n = 2$. This equation indicates that there exists a unique mapping between the operative n-value and the observed concentration response curve at some downstream station. Our goal is to employ this mapping in reverse to extract the operative n-value for the three-generation bifurcation model from experimentally measured response curves (such as those shown in Fig. 4). However, Eq. (3) only applies in straight-tube geometry. Complexities imposed by experiments in realistic lung geometries require additional refinements. In particular, four deviations must be addressed to sufficiently relate the theory for straight tubes to experiments in the bifurcation model:

1. Finite width of the interrogation region (thickness of the laser sheet) during LIF measurements.
2. Bandedness of the dye-containing regions during expiration experiments.
3. Mass conservation of the bolus traversing a branching experimental model.
4. Non-ideality of the initial bolus.

These points are discussed in the following three sections. To summarize, points 1 and 2 require theory to be supplemented with numerical simulations, point 3 can be accounted for with straightforward mass conservation equations, and point 4 requires the use of a dedicated calibration experiment to account for bolus non-ideality.

3.2. Numerical simulation

Eqs. (2) and (3) apply to an infinitesimally thin interrogation plane in the cross section of the tube. It is desirable to re-express the mean concentration distribution for a thin but finite axial width of interrogation corresponding to the laser sheet thickness (approximately 2 mm) during experiments. The net effect of this

interrogation volume is to slightly average concentration in the axial direction. It is convenient to implement this modification numerically.

Second, flow visualizations showed that only certain regions of the cross section contain dye on expiration (Fig. 6). For low-*Re* expiration, the images reveal well-ordered bands of dye-containing regions as shown schematically in Fig. 8. Precise delineation of these bands is based on ensuring equal areas within the cross section, since the model is in-plane and all daughters at a given generation have the same diameter (because each daughter has the same volume flow rate, an implicit assumption here is that the flow from each daughter tube occupies the same fraction of the cross-sectional area in the parent). Newton's method was employed to solve a transcendental equation for the boundaries of each region. At high *Re* on expiration, centrifugal effects mix solute throughout the half cross section. For all *Re* numbers on inspiration, dye completely filled the cross section. In summary, flow visualizations support dye-containing regions in the cross section based on the particular conditions. It is difficult to account for such bandedness with an analytical approach. On the other hand, a numerical method conveniently allows "painting" these specific regions in the cross section with dye.

An axisymmetric grid was implemented in the numerical method to represent the geometry of the straight tube. Non-uniform grid spacing was used in the radial direction to improve resolution nearer the tube circumference for higher order polynomials. Convergence studies were conducted to select the optimal grid resolution for each case. The initial bolus was "painted" into the grid. The interrogation region, comprised of the entire cross section with an axial width matching the thickness of the interrogating laser sheet, was placed at the desired distance downstream. An axisymmetric transport profile with polynomial of prescribed order was then used to deform the initial bolus as a function of time. The location of a given parcel of solute as a function of time was simply calculated as the product of velocity at that radial location and the duration of the flow. Each parcel of dye was tracked through the interrogation volume. At each time step, the average concentration within the interrogation region was calculated. In this manner, the average concentration of a bolus as a function of time (i.e., the response curve) in a tube with a known transport profile was obtained. Finally, the standard deviation was calculated from the numerical response curve.

Inputs to the numerical model include tube diameter, initial bolus description, interrogation distance (from injection) and width, and average flow velocity. The main parameter is the polynomial order of the transport profile. The output is standard deviation of the response curve. Sample response curves for $n = 1$–4 from the numerical are presented in Fig. 9. Note that as transport profiles become more plug-like (increasing n), solute reaches the interrogation station later and transits through it more quickly.

To summarize, Taylor's solution for the mean concentration of an initial disk of solute in Poiseuille flow was first extended to a general polynomial order, and subsequently implemented with a numerical model which accounts for a finite axial interrogation width (point 1), and a prescribed dye-containing band based on qualitative experimental observations (point 2).

3.3. Bolus mass conservation

In a branching network of tubes such as that used in the present study, the axial extent of a bolus changes due to a change in local cross sectional area. For example, on inspiration a bolus encounters an increase in local cross-sectional area of approximately 20% upon entering the first pair of daughter tubes. Mass conservation dictates a subsequent decrease in the axial length of the bolus. Cross-sectional area is further increased by 20% in the second and third generations for inspiration, with a concomitant decrease in the axial length of the bolus. Thus, we assume the bolus fills the entire cross section on inspiration and decreases in axial length according to the ratio of parent-to-daughter tube areas (1/1.2). The expression for local bolus length (X_G) at a particular generation (G) on inspiration, based on the initial axial bolus length (X_o), takes the form

$$X_G = \frac{1}{1.2^G} X_o. \tag{4}$$

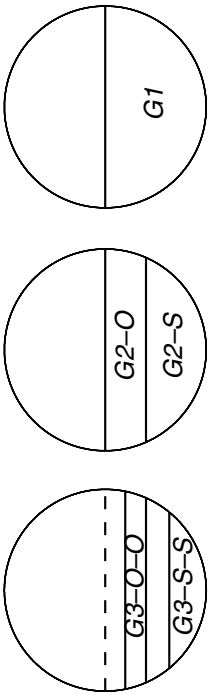

Fig. 8. Regions containing dye in the cross section at low *Re* during expiration which were used in numerical model. Top circle is for *G*1 analysis, middle circle for *G*2 cases (*G*2-*O* and *G*2-*S*), and bottom circle for *G*3 cases (*G*3-*O*-*O* and *G*3-*S*-*S*). Each sub-region in a particular circle possesses equal area (i.e., half of the cross section at *G*1, quarter at *G*2, and eighth at *G*3).

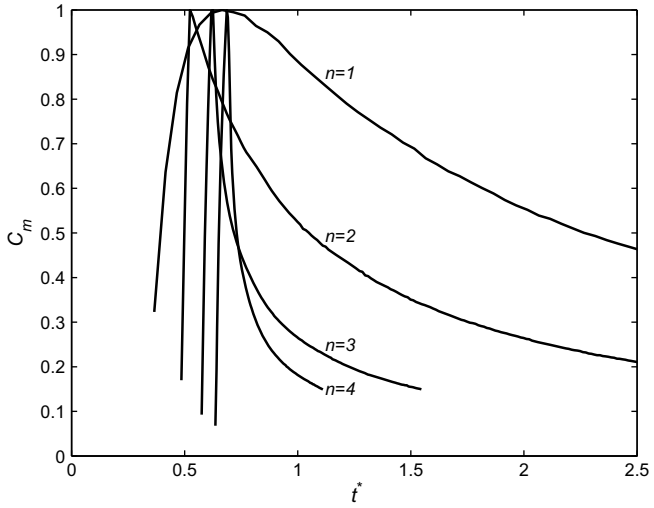

Fig. 9. Example of normalized mean concentration distribution curves from the numerical simulations. Notice later arrival and shorter transit time for more plug-like transport profiles. Time has been non-dimensionalized.

A similar phenomenon occurs on expiration, however, now only certain regions of the cross section contain dye, as shown in the qualitative experimental observations. Utilizing the area of the bands at low *Re*, the change in axial length of the bolus with generation for low *Re* expiration can be found as

$$X_G = 1.2^G X_o. \tag{5}$$

Assuming that dye filled half of the cross section for high *Re* expiration, the equation for axial length of the bolus at different generations is

$$X_G = \frac{1.2^G}{2^{G-1}} X_o. \tag{6}$$

These equations were applied in the numerical simulation for inspiration and expiration at various generations to ensure that the bolus mass was preserved thereby accounting for point 3.

3.4. Poiseuille flow calibration for non-ideality of bolus

The only outstanding concern prohibiting application of the *n*th order polynomial transport model to the bolus measurements is the non-ideal injection of the bolus (point 4). The transport profile model assumes an ideal cylindrical bolus, whereas in practice the bolus may appear more ellipsoidal. This deviation from non-ideality can have a significant effect on the shape of the response curve. Unfortunately, the exact three-dimensional shape of the injected bolus cannot be quantified *a priori*. While the previous three points have been addressed theoretically or numerically, the non-ideality of the injected bolus can only be removed by experimental calibration.

Calibration experiments were conducted using a straight-tube Poiseuille flow apparatus. Poiseuille flow constitutes a satisfactory benchmark because experiments may be conveniently conducted with a known transport profile polynomial, $n = 2$. The calibration experiments employed an identical bolus injection procedure as in the bifurcation experiments, and the response curves were obtained by probing with the same interrogation laser. Four cases were executed for calibration: two different bolus sizes in each of two tubes of different diameter. The average standard deviation of the response curves from multiple trials with a common set of experimental variables was calculated. The standard deviation was then compared with that obtained from the companion numerical simulations with $n = 2$ to evaluate the effect of bolus non-ideality. On average, the experimental standard deviation was 65% smaller than the numerical standard deviation. Thus, experimental response curves feature less broadening of concentration in time than predicted by numerical simulations.

This discrepancy may be attributed to the ellipsoidal rather than cylindrical nature of the initial slug of dye in practice. When the initial bolus is viewed in cross section, more solute exists near the centerline than near the tube walls. As a consequence, less solute is available at the "tails" (i.e., near-wall regions) of the transport profile when streaming through the interrogation station. The net result is to produce a more rapidly declining concentration distribution (narrower curve) which yields a relatively smaller standard deviation. The ratio between experimental and numerical standard deviations was implemented as a calibration factor to account for bolus non-ideality.

This calibration for the initial non-ideality of the bolus was only applied to analysis of inspiration. It was not possible to replicate the bandedness exhibited for expiration in a calibration experiment. However, the lack of availability of a calibration factor for the analysis of expiration is not a serious impediment because the factor is likely to be close to unity. This expectation is based on the trumpet-like nature of the cross-sectional area of the lung as a function of generation. Mass conservation on expiration states that the bolus becomes compressed radially, thereby radially shrinking minor imperfections in the initial bolus. Thus, the convergent nature of the expiration flow should reduce the effect of a non-ideal upstream distribution.

In summary, a Poiseuille flow apparatus was used to extract a calibration factor to account for the effect of a non-ideal initial bolus distribution on the experimental results for inhalation. The experimental difficulty in injecting an ideal bolus complicates the subsequently measured dispersion and may contribute to the variation in dispersion metrics reported in human subjects.

3.5. Summary of analysis technique for bifurcation experiments

The four deviations from theory have been accounted for as described in the previous section. It is now possible to extract the value of *n* for the transport profile from experimental response curves in bifurcating tubes with confidence as described next.

First, the ensemble average standard deviation of the response curves from experiments was obtained. Next, the same set of conditions was input to the numerical simulation and standard deviations were calculated for varying *n* (say, $1 \leqslant n \leqslant 10$). Remember that the numerical model accounts for the finite width of the laser sheet and the bandedness of the dye-containing region in the cross section, while the axial length of the bolus is adjusted using Eqs. (4)–(6). The experimentally obtained standard deviation is then multiplied by the calibration factor to account for bolus non-ideality. The last step is to interpolate the experimental value of standard deviation within the numerical values and look-up the corresponding value of *n*. In this manner, experiments and numerical simulations were reconciled to determine transport profiles.

While some details of the transport profile in the airways may be removed by assuming an *n*th order polynomial, the analysis still characterizes the overall shape of the transport profiles, providing a simple overall representation of dispersion in the airways. Also, the relative shape of transport profiles as a function of the independent variables (generation/branch, flow direction, *Re*) is valuable information.

4. Results and discussion

Experiments, simulations, and analyses were conducted in the manner described above. The end product of this effort was the transport profile, given in terms of the order of the polynomial *n*, for the flow through the model of the conductive airways as a function of the independent variables. The influence of generation/branch, flow direction, and *Re* was assessed by grouping results within each category for presentation.

Fig. 10 shows the polynomial order of the transport profile for generations one, two and three. A legend further provides the particular branch at the given generation and flow direction. Note that no discrimination is made based on *Re*. For example, two data points, one each for low and high *Re*, exist for inspiration after one generation (inspiration-*G*1).

The most striking feature of Fig. 10 is the relative independence of the transport profile with generation and branch. For all branches investigated at generations one, two and three, the polynomial order of the transport profile is approximately three. Apparently, the convective dispersion in one generation is typical of all generations for these *Re* values in the conducting airways. Whether the direction of the secondary currents remains the same in subsequent generations or changes direction, explored in the family of *S* and *O* cases, does not seem to affect convective dispersion. Local conditions dominate the history of the flow.

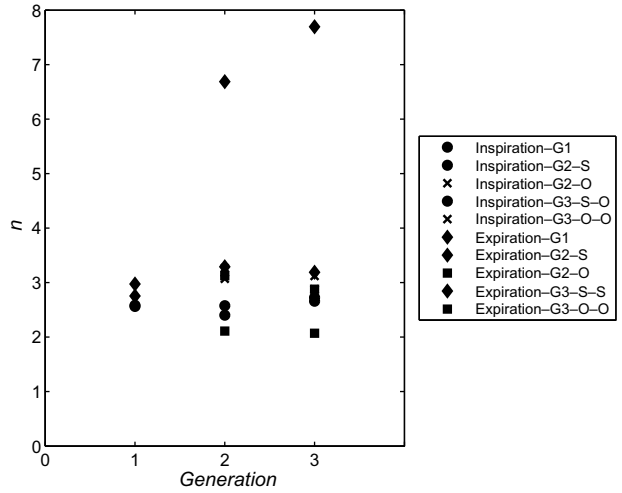

Fig. 10. Polynomial order of transport profile for various generation/branch combinations.

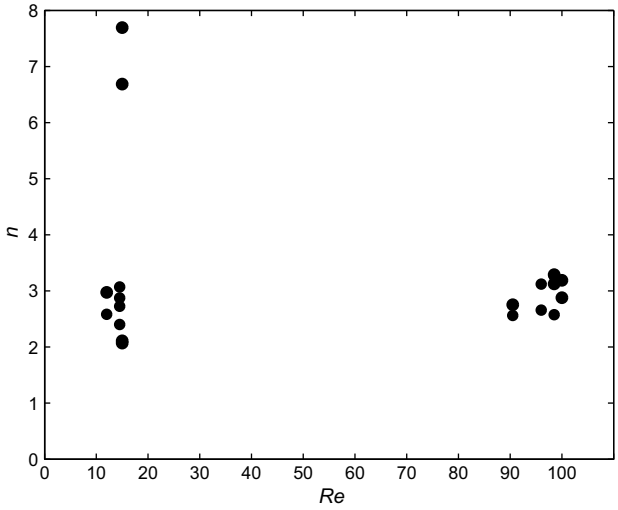

Fig. 12. Polynomial order of transport profile for various *Re*.

Only two data points in Fig. 10 deviate from a magnitude of approximately three; those for *G2-S* and *G2-S-S* on expiration at low *Re*. These data indicate some inadequacy in the assumed region of the cross section containing dyed fluid for the *S* case of expiration at low *Re*. It is likely that the dyed regions in the experiments did not exactly match those in the simulations. These outliers are also evident in the following two figures.

Next, the transport profiles are given in Fig. 11 as a function of flow direction. Results are grouped only by inspiration and expiration, regardless of generation/branch history and *Re*. These data indicate that transport profiles for both inspiration and expiration are approximately three for this *Re* range. Neither the splitting/merging nature of the flow nor the presence of two/four vortices at high *Re* on inspiration/expiration seems to affect the results. This finding bears on the nature of steady streaming in the airways. How can steady streaming occur in the airways if the transport profile is approximately the same on inspiration and expiration? It will be discussed in greater detail shortly that the irreversibility producing steady streaming may be attributed in part to the branching geometry of the airways.

The impact of *Re* on convective dispersion is revealed in Fig. 12. Results were grouped without regard to generation/branch or flow direction. Again, transport profiles do not vary with the independent variable, *Re*. This finding is somewhat surprising in light of the fact that none, two, or four secondary vortices (as shown in Figs. 5 and 6) may be present in the results given in the figure. Secondary activity in general does not affect transport profiles on inspiration or expiration in the conducting airways at these *Re*. This discovery has implications to simple streaming and augmented dispersion.

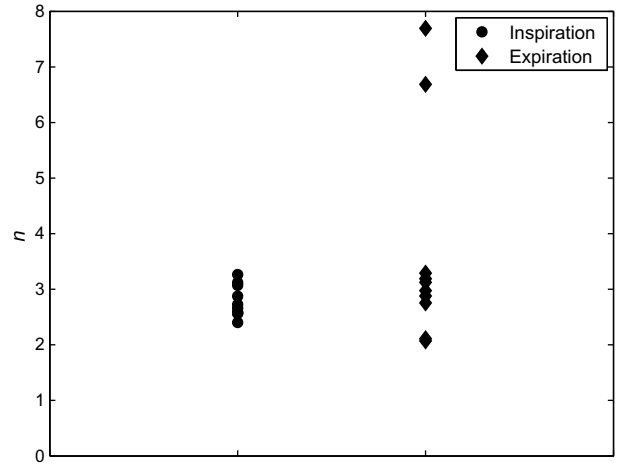

Fig. 11. Polynomial order of transport profile on inspiration and expiration.

5. Conclusions and implications

Transport profiles measured in these experiments are due exclusively to convection. Dispersion happens by the deformation of a passive tracer which precisely follows flow streamlines. For this reason, results do not include the effects of Brownian diffusion for gases or Brownian diffusion, particle inertia, and gravitational settling for aerosols. This study is most applicable to the dispersion of particles with low intrinsic mobility. The relative strength of transport due to molecular diffusion with respect to convection may be evaluated through the Peclet number $\left(Pe = \frac{ud}{D_{\text{mol}}}\right)$. Here, u is the average flow velocity. Implementing the definition of the Peclet number along with the symmetric Weibel model for normal respiration illustrates that diffusion may only be important in the last few generations for particles around 0.5 μm in diameter. For gases, however, molecular diffusion is comparable in strength with convection in the peripheral airways. These considerations must be remembered when interpreting results of this effort.

A broad look at all results for the transport profile reveals that $n \sim 3$, regardless of generation/branch history, flow direction, or *Re*. In general, the convective transport profile in the airways may be slightly more blunted than that for Poiseuille flow. The flow in the conducting airways on inspiration and expiration at $10 \leqslant Re \leqslant 100$ possesses a few features which may produce $n \sim 3$ for the transport profile. At low *Re*, viscous effects guarantee a flow similar to Poiseuille flow. Depending on *Re* and local geometry, secondary currents and undeveloped flow (due to boundary layer growth) may result in a transport profile slightly more blunted than that for Poiseuille flow. Another factor which may increase *n* over Poiseuille flow, even for low *Re*, is the cross-sectional area change of the bifurcations (circular-elliptical-dumbbell).

Figs. 5 and 6 show that transport is mainly parallel to the tube axis at Re = 10 and features some secondary activity at Re = 100. Transport profiles at low and high *Re* in Fig. 12, however, are similar. Secondary flows are not significant enough at *Re* = 100 to greatly alter the distribution of mass from *Re* = 10. Simple streaming must dominate augmented dispersion in the conducting air-

ways for $Re \leqslant 100$ for both inspiration and expiration. Thus, mass transports through the respiratory tract via simple streaming, with an effective transport polynomial of order $n \sim 3$, for approximately generations 7–16 of the symmetric Weibel model during normal respiration.

For $Re \sim 1000$ (proximal to generation 6 of the symmetric Weibel model during normal respiration), augmented dispersion may be important. Effective diffusivity (D^*) is another metric of convective dispersion besides the transport profile. Scherer et al. [23] measured the effective diffusivity in a five-generation model of the airways. Clear separation between results for inspiration ($D^* = 1.08ud$) and expiration ($D^* = 0.37ud$) at $Re \sim 1000$ was observed. The results of Scherer et al. [23] suggest that n is smaller on inspiration than expiration due to secondary currents (in agreement with Park and Wexler [21]), since D^* was larger for inspiration than expiration. At $Re \sim 1000$, the quadruple vortex on expiration may produce a more blunted transport profile than the double vortex on inspiration.

The preceding explanations of transport mechanisms pertain only to steady flow in the airways, whereas respiration is cyclical. The next step is to examine the results with respect to steady streaming. The present study has found $n \sim 3$ for both inspiration and expiration for all inspected generation/branch histories and Re. Since n is the same for inspiration and expiration, steady streaming cannot be explained on the basis of differing transport profiles in a given tube. Rather, these data suggest steady streaming in the airways is due to similar transport profiles interacting in a bifurcating tube geometry. Geometrical asymmetries in a bifurcation, not dissimilar velocity profile in a single tube, drive steady streaming. This phenomenon is akin to the steady streaming obtained in studies with tapered channel geometry [24]. Steady streaming in the lung due to geometrical asymmetries also removes the burden of proof from velocity profiles at lower Re. The majority of the conducting region of the lung for normal and vigorous respiration is at $Re \leqslant 100$. As Re decreases to zero, well-founded fluid mechanical principles guarantee that velocity profiles in a single tube will be reversible.

An illustration is provided in Fig. 13 to visualize the interaction of similar-shaped transport profiles and the net result on steady streaming. A transport profile on inspiration is shown in the parent tube and transport profiles on expiration are shown in both daughter tubes. The effective transport profile on expiration, averaged over the cross section of *both* tubes with $n \sim 3$, is blunter than $n \sim 3$. The resultant transport profile after a cycle, due to the interaction of the inspiratory profile with $n \sim 3$ and the effective expiratory profile with $n > 3$, is presented at the tri-section of the three tubes. The magnitude of the polynomial order for the inspiratory transport profile is lower than the polynomial order for the effective expiratory transport profile, which agrees with Park and Wexler [21]. Furthermore, the resultant transport profile due to combining an inspiratory profile in the parent tube with two expiratory profiles in the daughter tubes has a shape in agreement with the data of Haselton and Scherer [12,13] for Re as low as unity. Solute originally near the centerline is advected away from the "mouth" and that near the tube walls toward the "mouth" after one cycle. Note that this conception of steady streaming obeys mass conservation as equal fluxes pass through a control surface in the cross section on inspiration and expiration.

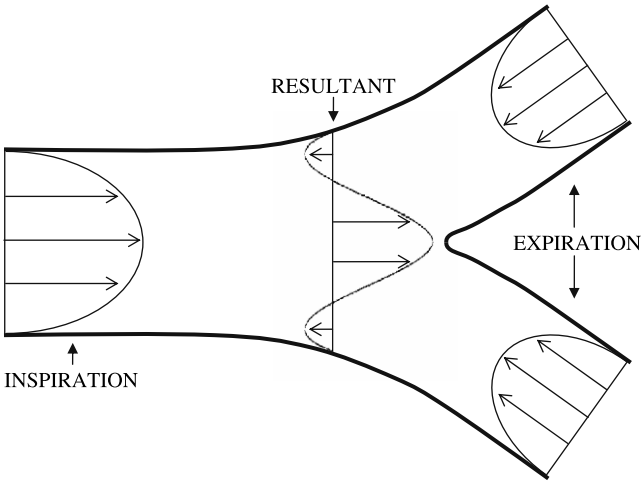

Fig. 13. Illustration of steady streaming due to bifurcation geometry.

Dispersion during steady inspiration and expiration has been quantified in this analysis. Over a complete cycle, however, some amount of the original bolus reassembles. Thus, assuming independent dispersion on inspiration and expiration is an overestimate. Assessing steady streaming facilitates a more realistic description of dispersion over a respiratory cycle. While these assessments have not been explicitly performed herein, the phenomenon offered to explain steady streaming suggests asymmetry in airway geometry (e.g., area ratio, branch angle and radius of curvature) is more important to the magnitude of steady streaming than the asymmetry in velocity profiles.

Additionally, steady streaming may be affected to some degree by the anchoring of mass at each bifurcation due to the action of the no-slip boundary condition as the tip of the bolus impacts the carina on inspiration [14,15]. The influence of this phenomenon on overall convective dispersion, and relative magnitude with respect to steady streaming by geometrical asymmetry proposed herein, remains to be seen. Transitory effects, as seen by Moskal and Gradon [25], may also contribute to steady streaming, however, particle image velocimetry measurements [11] suggest little mixing at flow reversal for these Re.

The results of this effort may also clarify the mechanisms by which HFV achieves ventilation with tidal volumes less than the dead space. As stated, steady streaming may be due to geometric asymmetries associated with a bifurcating network of tubes. Therefore, regardless of Re, the branching nature of the lung produces a net flux of species during each cycle. By this argument, steady streaming is not confined to a few generations of the airways nearer the trachea, but rather acts throughout the respiratory tract. Furthermore, one-way dispersion is dominated for $Re \leqslant 100$ by simple streaming. Solute is mainly displaced along the axis of the tube, not mixed laterally by secondary currents. Transport parallel to the tube axis serves to maximize axial dispersion during steady streaming. The action of steady streaming over the entire respiratory tract, coupled with optimal transport (parallel to tube axis), implies steady streaming may play a key role in HFV. This argument is further supported by the Peclet number, which is greater than one for oxygen in air up to generation 17 in the symmetric Weibel model during HFV.

Acknowledgements

Research described in this article was supported by Philip Morris USA Inc. and Philip Morris International.

References

[1] M. Kohlhaufl, P. Brand, T. Selzer, G. Scheuch, T. Meyer, N. Weber, H. Schulz, K. Haussinger, J. Heyder, Diagnosis of emphysema in patients with chronic bronchitis: a new approach, Eur. Respir. J. 12 (1998) 793–798.
[2] D.A. Edwards, C. Dunbar, Bioengineering of therapeutic aerosols, Annu. Rev. Biomed. Eng. 4 (2002) 93–107.
[3] R.J. Robinson, C.P. Yu, Deposition of cigarette smoke particles in the human respiratory tract, Aerosol Sci. Technol. 34 (2001) 202–215.

[4] J. Schwartz, D.W. Dockery, Increased mortality in Philadelphia associated with daily air pollution concentrations, Am. Rev. Respir. Dis. 145 (1992) 600–604.
[5] D.A. Edwards, J.C. Man, P. Brand, J.P. Katstra, K. Sommerer, H.A. Stone, E. Nardell, G. Scheuch, Inhaling to mitigate exhaled bioaerosols, Proc. Natl. Acad. Sci. 101 (50) (2004) 17383–17388.
[6] J.M. Drazen, R.D. Kamm, A.S. Slutsky, High-frequency ventilation, Physiol. Rev. 64 (2) (1984) 505–543.
[7] C. Darquenne, P. Brand, J. Heyder, M. Paiva, Aerosol dispersion in human lung: comparison between numerical simulations and experiments for bolus tests, J. Appl. Physiol. 83 (3) (1997) 966–974.
[8] J. Heyder, J.D. Blanchard, H.A. Feldman, J.D. Brain, Convective mixing in human respiratory tract: estimates with aerosol boli, J. Appl. Physiol. 64 (3) (1988) 1273–1278.
[9] J.J. Fredberg, Augmented diffusion in the airways can support pulmonary gas exchange, J. Appl. Physiol. 49 (2) (1980) 232–238.
[10] F.E. Fresconi, A.S. Wexler, A.K. Prasad, Expiration flow in a symmetric bifurcation, Exp. Fluids 35 (2003) 493–501.
[11] F.E. Fresconi, A.K. Prasad, Secondary velocity fields in the conducting airways of the human lung, J. Biomech. Eng. 130 (1) (2008) 011015–011024.
[12] F.R. Haselton, P.W. Scherer, Bronchial bifurcations and respiratory mass transport, Science 208 (1980) 69–71.
[13] F.R. Haselton, P.W. Scherer, Flow visualization of steady streaming in oscillatory flow through a bifurcating tube, J. Fluid Mech. 123 (1982) 315–333.
[14] D.Y. Lee, J.W. Lee, Dispersion of aerosol bolus during one respiration cycle in a model of lung airways, J. Aerosol Sci. 33 (2002) 1219–1234.
[15] F.E. Fresconi, A.K. Prasad, Convective dispersion during steady flow in the conducting airways of the human lung, J. Biomech. Eng. 129 (5) (2007) 722–732.
[16] T.J. Pedley, Pulmonary fluid dynamics, Annu. Rev. Fluid Mech. 9 (1977) 229–274.
[17] E.R. Weibel, Morphometry of the Lung, Springer-Verlag, Berlin, 1963.
[18] L.M. Hopkins, J.T. Kelly, A.S. Wexler, A.K. Prasad, PIV measurements in complex geometries, Exp. Fluids 29 (1) (2000) 91–95.
[19] Y. Zhao, B.B. Lieber, Steady expiratory flow in a model symmetric bifurcation, J. Biomech. Eng. 116 (1994) 318–323.
[20] Y. Zhao, B.B. Lieber, Steady inspiratory flow in a model symmetric bifurcation, J. Biomech. Eng. 116 (1994) 488–496.
[21] S.S. Park, A.S. Wexler, Particle deposition in the pulmonary region of the human lung: a semi-empirical model of single breath transport and deposition, J. Aerosol Sci. 38 (2007) 228–245.
[22] G.I. Taylor, Dispersion of soluble matter in solvent flowing slowly through a tube, Proc. R. Soc. Lond. A 219 (1953) 186–203.
[23] P.W. Scherer, L.H. Shendalman, N.M. Greene, A. Bouhuys, Measurement of axial diffusivities in a model of the bronchial airways, J. Appl. Physiol. 38 (4) (1975) 719–723.
[24] D.A. Godleski, J.B. Grotberg, Convection-diffusion interaction for oscillatory flow in a tapered tube, J. Biomech. Eng. 110 (1988) 283–291.
[25] A. Moskal, L. Gradon, Temporal and spatial distribution of aerosol particles in the upper human airways during breathing cycles, J. Aerosol Sci. 33 (2002) 1525–1539.